Superior Imaging Performance of All-Fiber, Two-Focusing-Element Microendoscopes

Karol Karnowski , Gavrielle Untracht , Michael Hackmann , Onur Cetinkaya , and David Sampson , *Fellow, IEEE*

Abstract—All-fiber-optic imaging microendoscopes are emerging as an important tool in bioimaging studies, including those conducted with optical coherence tomography, but physical limitations constrain the achievable beam characteristics of designs using a single focusing element. These constraints are especially relevant for applications that require a long working distance, high resolution, and/or minimal probe diameter. Through detailed analysis based on ABCD matrix modelling, we show that side-viewing probes combining a graded-index (GRIN) fiber with a ball lens – GRIN-ball-lens probes (GBLPs) – offer superior performance over a range of numerical apertures and pave the way for a broader range of imaging applications. The performance of side-viewing GBLPs designed for 1300-nm optical coherence tomography imaging is compared against commonly used single-focusing-element all-fiber side-viewing probe designs, namely, ball-lens probes (BLPs) and GRIN-fiber probes (GFPs). All possible realizations of this novel probe design and their impact on the requisite design tradeoffs are investigated, including the impact on probe performance of fabrication error and the refractive index of the surrounding medium. Applications of GBLPs, including ultra-high-resolution (sub-2 micrometer) miniature probes for micro-endomicroscopy, are discussed.

Index Terms—Fiber optics, optical fiber, optical fiber applications, high-resolution imaging, biomedical optical imaging, optical coherence tomography, probes, endoscopes, optical imaging, optical microscopy.

Karol Karnowski is with the Institute of Chemistry, Polish Academy of Science, 00-901 Warsaw, Poland, with the International Centre for Translational Eye Research, 00-901 Warsaw, Poland, and also with the The Optical + Biomedical Engineering Laboratory, University of Western Australia, Perth 6907, Australia (e-mail: kkarnowski@ichf.edu.pl).

Gavrielle Untracht is with the The Optical + Biomedical Engineering Laboratory, University of Western Australia, Perth 6907, Australia, and also with Surrey Biophotonics, School of Biosciences & Medicine and Advanced Technology Institute, University of Surrey, Guildford GU2 7XH, U.K. (e-mail: g.untracht@surrey.ac.uk).

Michael Hackmann is with the The School of Human Sciences, University of Western Australia, Perth 6907, Australia, and also with the The Optical + Biomedical Engineering Laboratory, University of Western Australia, Perth 6907, Australia (e-mail: michael.hackmann@research.uwa.edu.au).

Onur Cetinkaya is with the Polish Academy of Science, 00-901 Warsaw, Poland, and also The Optical + Biomedical Engineering Laboratory, University of Western Australia, Perth 6907, Australia (e-mail: ocetinkaya@ichf.edu.pl).

David Sampson is with Surrey Biophotonics, School of Biosciences & Medicine and Advanced Technology Institute, University of Surrey, Guildford GU2 7XH, U.K. (e-mail: d.sampson@surrey.ac.uk).

Digital Object Identifier 10.1109/JPHOT.2022.3203219

I. INTRODUCTION

MINIATURIZED fiber-optic probes, or micro-endoscopes, are enabling bioimaging studies of tissue microstructures deep within a sample or patient [1], [2], [3]. While such probes can be used with a range of imaging modalities, endoscopic optical coherence tomography (OCT) has emerged as a promising technique for volumetric imaging inside of both solid tissues [4], [5] and hollow organs. We can distinguish three major regimes of fiber-optic probe operation. Studies of large, hollow organs (e.g., upper airway [6],) require the largest imaging depth ranges (up to 15 mm or more [7]), which are usually achieved by using low-resolution Gaussian beams. The specific requirements for the beam diameter are typically subordinated by the need for a long working distance and diameters on the sample surface vary from 30 μm to more than 100 μm depending on the airway inner diameter. An intermediate resolution range (10–30 μm) is useful for a wider range of applications, including imaging in the esophagus, small airways, blood vessels, bladder, ovaries, or the ear canal [8], [9], [10]. The range that is most challenging to design and implement corresponds to high-resolution beams smaller than 10 μm. Imaging probes with resolution better than 10 μm would advance some of the current intermediate-resolution application areas, are potentially useful for animal model studies (especially when small animals are considered), and will facilitate practical deep-tissue microscopy through needle probes [9].

When designing a probe for a given application, the tradeoffs between the design parameters and their effect on imaging performance must be considered [11]. In most instances, optimizing the design for one parameter sets limits on the range of the other parameters. For example, in the case where a single refractive lens with a given focal length, *f*, is used, the numerical aperture, NA, describes the link between the lens diameter, *D*, and the achievable resolution: NA $\approx \frac{nD}{2f}$, where *n* is the refractive index of the medium surrounding the probe (which is often a liquid or biological tissue). High-numerical aperture, high-resolution optics tend to have a shorter working distance (WD); better resolution and longer working distance are both more difficult to realize as the probe diameter is decreased. This can be especially problematic for side-viewing probes, which are advantageous

for small-diameter volumetric imaging applications. For side-viewing probes, relative to their forward-viewing equivalents, a larger minimum working distance is required to ensure that the focal spot is outside of the imaging probe due to the extra pathlength required to deflect the beam [3]. This problem is exacerbated if the imaging probe is encased in a catheter or needle, thereby extending (by the wall thickness of the casing) the minimum working distance required. For some applications, the working distance has become a limiting factor in terms of the minimum achievable resolution or probe diameter [6], [12].

In contrast to the greater optical design challenge presented by smaller probe diameters, most applications benefit from minimizing the probe diameter because of reduced perturbation to the sample and/or trauma to the patient [13]. This remains true even in the case of imaging large hollow organs as a smaller probe size will permit smaller, more flexible catheters which contribute to patient tolerance. One means of achieving small diameters is by using monolithic, all-fiber-optic probes – for which the diameter is limited only by the optical fibers themselves. In addition to achieving minimal probe diameters, such probes benefit from their ease of fabrication, via fusion splicing technology, thereby avoiding the need for discrete alignment and fixation of individual micro-optical components. Designs based on two types of focusing elements have emerged as the most common: GRIN-fiber probes (GFPs) [14], [15] and ball-lens probes (BLPs) [16], [17]. GRIN-fiber probes are easy to fabricate, and the GRIN refractive power is not lost when the refractive index of the surrounding medium approaches that of the probe, but achievable designs are limited by the commercially available fibers. It is particularly challenging to achieve high-resolution designs for GRIN fibers with a small core size. For side-viewing probes, the curved surface of the fiber (and potentially catheter) introduces astigmatism which can be detrimental to the imaging performance. Spherical BLPs do not suffer from astigmatism, but a ball size larger than the fiber diameter is often required to achieve a comparable resolution to the GFP. Additionally, the focusing power of the BLP depends on the refractive index of the surrounding medium, an important consideration when working in an index-matching medium or in close contact with biological samples. Particularly for applications that require small focal spot sizes and/or long working distances, the range of achievable probe performance parameters using either of these designs is limited.

One approach to expand the performance parameter range of achievable designs, borrowed from the design of bulk optics, is to use multiple refractive elements – similar to the approach used in the design of long-working-distance objective lenses [18]. This idea was recently explored in [19] for designing long-working-distance probes for low-NA imaging of large airways. In fact, combining multiple focusing elements offers superior performance over a wider range of NAs and for many other imaging regimes and targets. Probes with multiple focusing elements can achieve better resolution with a smaller diameter and can achieve longer working distances without sacrificing resolution. Indeed, the use of multiple GRIN fiber segments within one probe has been investigated to achieve an extended depth of field for OCT imaging [20], [21].
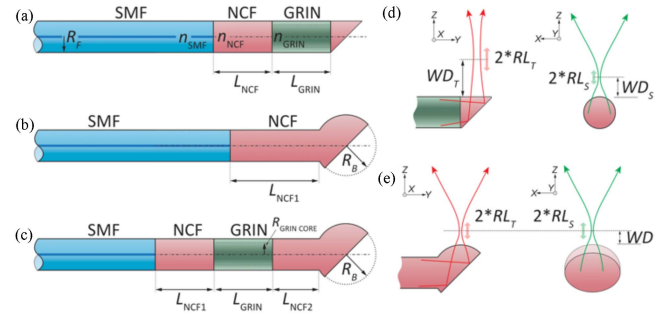

Fig. 1. Schematic of monolithic designs for common side-viewing optical probes and the hybrid GRIN-fiber and ball-lens design. (a) Fiber probe with graded-index (GRIN) fiber as the refractive element. (b) Fiber probe with ball lens fabricated on the tip of no-core fiber (NCF). (c) Fiber probe where GRIN fiber is used to pre-shape the beam before it reaches a ball-lens element. (d) and (e) Probe output beams presented for tangential (red rays) and sagittal (green rays) planes for GRIN probe and BL probes, respectively. R_F, $R_{\text{GRIN CORE}}$, R_B – radii of single-mode fiber (SMF), core of GRIN fiber and ball lens, respectively; n_{SMF}, n_{NCF}, n_{GRIN} – refractive index of SMF, NCF and GRIN fiber, respectively; L_{NCF}, L_{NCF1}, L_{GRIN}, L_{NCF2} – lengths of fiber sections of NCF and GRIN fiber; $WD_{T,S}$ and $RL_{T,S}$ – working distance and Rayleigh length in tangential and sagittal planes of the probe, respectively.

In this study, we demonstrate that all-fiber, two-refractive-element probes, which employ both a segment of GRIN fiber and a ball lens – hereafter termed GRIN-ball-lens probes (GBLPs) – greatly enhance the performance of monolithic all-fiber probes. We compare GBLPs in detail with the most-used GRIN-fiber probe and ball-lens probe designs. We investigate the advantages in performance, particularly for applications which require longer working distances, better resolution, and/or small probe size. Finally, we explore a range of applications expected to benefit from the use of GBLPs, particularly the development of micro-endomicroscopes for minimally invasive, cellular-resolution imaging [11].

II. METHODS

The GFP (Fig. 1(a)) consists of single-mode fiber (SMF) connected to a no-core fiber (NCF) section for beam expansion, then to a GRIN fiber section for focusing, and a second NCF section that is terminated in an angled facet to enable side-viewing operation. As the beam exits via the fiber sidewall, which acts as a cylindrical lens, the difference between the sagittal (x-z) plane (curved interface) and tangential (y-z) plane (flat interface) causes astigmatism (Fig. 1(d)). The BLP consists of an SMF and then a section of NCF for beam expansion but does not contain a GRIN focusing element; instead, a curved refractive surface (a ball lens), usually fabricated from NCF, is used to focus the beam (Fig. 1(b)). The ball lens at the fiber tip, if fabricated properly, is perfectly spherical leading to an anastigmatic output beam (Fig. 1(e)). Similar to the GFP, the ball lens element contains an angled planar facet to provide a side-viewing operation.

A schematic of a double-refractive-element all-fiber probe is depicted in Fig. 1(c). The GBLP takes full advantage of the anastigmatic BLP design. In contrast to the BLP, where only a diverging beam can be delivered to the curved interface of the ball lens, the GBLP utilizes an additional section of GRIN fiber to pre-shape the beam before it reaches the ball-lens section. As

TABLE I
PARAMETERS OF AND SIZE RANGES FOR FIBER COMPONENTS USED IN
SIMULATIONS

#	Element/fiber type		Parameters	Range
1	NCF		n=1.447	GIF: $0-500$ μm DRAKA: $0-800$ μm
2	GRIN	GIF625	n_{core}=1.475 g=4.1/mm 62.5/125 μm core/cladding diameter $L_{pitch}\cong 1.53$ mm	$0-0.4\ L_{pitch}$
		DRAKA ELITE	n_{core}=1.479 g=6.224/mm 100/125 μm core/cladding diameter L_{pitch}=1 mm	
3	2nd NCF		n=1.447	$0-1000$ μm
4	Ball lens (NCF)		n=1.447	$2*R_B$ (R_B=76 μm$-R_{B\ max}$) $R_{B\ max}$= 190 μm

L_{pitch} – pitch length of the GRIN fiber, n – refractive index, n_{core} – refractive index of GRIN fiber core, g – gradient constant of GRIN fiber, R_B – radius of ball lens, $R_{B\ max}$ – maximum radius of ball lens.

will be shown in Section III, the additional focusing element used in the GBLP provides superior performance over the entire range of probe NAs when compared with GFP and BLP designs.

A. ABCD Matrix Simulation

Numerical simulations of the beam propagation for all probes under investigation are based on the matrix transformation of a Gaussian beam (ABCD matrix transfer theory) [22] using software we developed in MATLAB R2020b (*Mathworks,* USA). The beam passing through the probe is represented by a complex beam parameter. Each probe section (including fiber sections, interfaces between fiber types, and output probe interfaces) is described by an appropriate ABCD transmission matrix which is applied to the complex beam parameter. The performance of the modelled probe is characterized by the parameters: spot diameter (SD); working distance (WD); and confocal parameter (CP), defined as twice the Rayleigh length (RL).

In this study, we focused on all-fiber imaging probes designed for a central wavelength of 1300 nm as this wavelength is common for many OCT applications. Additionally, we do not expect large changes in performance trends for probes of the same design operating at other wavelengths. In Table I, we summarize the parameters and size ranges for fiber components used in our ABCD matrix simulations. We included two commercially available GRIN fibers: GIF625 (*Thorlabs*, USA) and DRAKA ELITE (*Prysmian Group*, Italy). The range of NCF lengths is different for the two fibers since they have different core diameters. An NCF length of 500 μm and 800 μm, for GIF625 and DRAKA fibers, respectively, corresponds to a beam diameter at the input of the GRIN fiber equal to the fiber core size. It is worth noting that the GRIN fiber with the smaller core diameter (GIF625) is reported to have a near-perfect parabolic refractive index profile, whereas many other GRIN fibers suffer from a central dip in the refractive index profile that impacts performance and the accuracy of ABCD matrix simulations [23]. The impact of imperfections in the refractive-index profile is not the focus of this study and has not been accounted for. However, we believe that comparing GRIN fibers with different core diameters can provide interesting results and conclusions.

The lengths of GRIN fiber sections in the following are given as a fraction of a GRIN pitch length ($L_{pitch} = 2\pi/g$, where g is the gradient constant of GRIN fiber). The refractive index of the GRIN fiber core and g parameter were determined by fitting the GRIN profiles to the experimentally measured beam profiles for various GRIN sections spliced to SMF fiber [23]. We note that the gradient parameter may vary for different batches of the same fiber from the same manufacturer. Therefore, it is recommended that the gradient parameter be measured for the specific GRIN fiber used. The NCF used for all simulations was FG125LA (*Thorlabs*, USA). The range of GRIN pitch reported from the simulation was chosen empirically to be 0–0.4. For GRIN pitches >0.4, we did not observe any improvements in probe performance.

Unlike for the first NCF section, we were not able to precisely predict the upper limit of the second NCF section length since it depends on the divergence of the beam exiting the GRIN fiber segment. Therefore, the 2nd NCF section was simulated for lengths up to 1 mm based on our experience with GFPs. It must be noted here that our simulation automatically excluded from results those cases where the beam diameter was larger than the GRIN core size or the size of the second NCF cross-section.

Ball lens sizes included in the simulated results were those that we were able to accurately and repeatably fabricate with an ordinary fusion splicer (e.g., Ericsson FSU 995). The largest simulated ball lens radius of 190 μm falls well within the sub-500-μm size limit we have previously set for micro-endomicroscopes and can fit easily within catheter tubing that has an outer diameter below this limit [11]. Smaller ball lenses could be fabricated; however, these designs typically have very short working distances and are often impractical to use.

For GFP and BLP, two design parameters were varied (1st NCF length and GRIN length for GFP, and 1st NCF and ball-lens radius for BLP) with a simulation step number n = 2000. The GBLP simulations were run for four variables (1st NCF length, GRIN length, 2nd NCF length, ball-lens radius) with a reduced simulation step nuumber (n = 150 for each varied parameter).

III. RESULTS

The most common approach to visualizing the probe performance is by mapping the output beam parameters (spot diameter and working distance) as a function of the diameter of the ball lens and the length of the NCF section. Such results for the BLP are presented in Fig. 2(a), (b). We consider as useful only probe
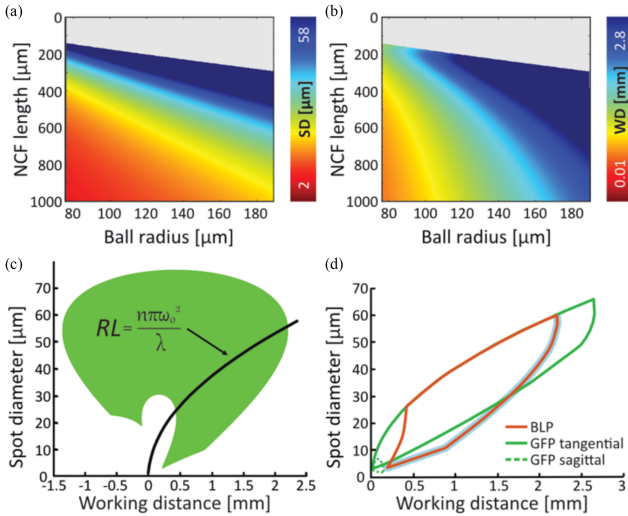
Fig. 2. Simulation results for BLP of spot diameter (a) and working distance (b) vs. NCF fiber length and radius of the ball lens. (c) Novel scatterplot visualization of the same BLP performance (spot diameter - SD and working distance - WD) covering the whole range of lengths and sizes of all probe components included in (a). The curve representing Rayleigh length (*RL*) as a function of spot diameter separates useful probe designs (meeting the working distance criterion, i.e., to the right of the black RL curve) from designs for which the depth range defined by the confocal parameter (CP) sits partially or entirely inside the probe. (d) Comparison of performance of BLP (solid red curve) and GFP for tangential (solid green curve) and sagittal (dotted green curve) planes extracted from corresponding scatterplots. Most of the further comparison will focus on the optimal working distance provided by the probe (thick light blue curve).

designs for which the focal plane is outside the probe and meet the criterion:

$$WD - RL \geq 0. \tag{1}$$

The imaging performance for OCT probe designs which do not meet (1) is limited because the CP determines the axial imaging range in OCT and part of the imaging range would fall within the probe itself. Probe realizations that do not meet (1) are masked out (grey color in Fig. 2(a), (b)). For the BLP, when the NCF section is too short, the beam does not expand sufficiently to be focused by the ball lens' spherical surface. In those cases, the output beam is either collimated or diverging.

Visualization as presented in Fig. 2(a)–(b) provides insight on the output beam parameters if only two parameters are varied (e.g., lengths of two probe components or one component and radius of the ball lens fabricated on the probe tip). However, in the case when more variables are used in simulation, such representation is not possible. For instance, the GBLP design consists of four major components: NCF spacer, GRIN fiber, 2nd NCF spacer and ball lens (Fig. 1(c)). Therefore, we introduce a novel alternative visualization of the probe performance that emphasizes the most interesting performance features in one comprehensive plot. Instead of color-mapping SD and WD separately, we plot spot diameter as a function of working distance using a scatter plot. Every realization that is a result of simulation over all chosen parameters (e.g., NCF length, GRIN length, ball-lens radius) is plotted as a single point in the space

of possible designs with the tradeoff of losing direct access to the design parameters. Instead, one can choose desired probe performance from the plot and from the model link it back to the design parameters. The scatter plot in Fig. 2(c) represents the overall performance of the BLP before taking (1) into account.

If we reject probe realizations that do not meet the working distance criterion, we include only scatter points on the right side of the curve corresponding to the Rayleigh length and spot diameter relation (black curve in Fig. 2(c)). To simplify comparison and quantitative analysis, only the boundary of the remaining useful scatterplot area (extracted using the MATLAB *boundary* function) is used in the following figures and discussion. In Fig. 2(d), such boundary plots for BLP (red) and GFP (green) are compared. For direct comparison of probe performance from the perspective of the longest working distance, only the right edge of the scatterplot is used (thick blue curve in Fig. 2(d)). From the comparison of scatterplots for the GFP and BLP, we see that the BLP provides longer working distances for spot diameters up to 30 μm, which covers most of the applications of OCT. This remains true as long as the probes are operated in air (discussed further in Section IV.C.)

With this novel visualization, one can clearly see the difference in GFP performance along tangential and sagittal planes (Fig. 2(d) bounded by solid green and dotted green curves, respectively). The additional small-radius curved surface at the sagittal interface reduces the range of possible probe designs to small spot diameters and very short working distances. Thus, the GFP, unlike its bulkier GRIN lens counterpart, has limited applications when working in air (the performance will improve when a refractive index-matching medium is used). For further investigation, we decided to use only the tangential plane results for GFP as the best ones for this probe type as well as representing the forward viewing version of the GFP probe.

A. GBLP vs. BLP and GFP

Essentially, the GBLP corresponds to the BLP with an additional GRIN fiber section which controls the divergence of the beam as it enters the ball lens. Therefore, not only diverging (as for BLP) but also pre-collimated or pre-focused beams can reach the curved exit surface of the probe. This pre-shaping of the Gaussian beam propagating within the probe results in superior performance and a larger range of possible probe designs of the GBLP (bounded by blue curve in Fig. 3(a)) when compared with BLP and GFP (red and green curves, respectively, in Fig. 3(a)).

One advantage of the GBLP is the ability to achieve longer working distances for those smaller diameter probes with low NA and large spot sizes. This has already been experimentally verified for OCT imaging in the upper airway [19]; similar imaging performance cannot be achieved using a GFP or BLP with the same small footprint. Such low-NA performance is possible using GRIN lenses; however, discrete lenses are bulkier and fabricated into a probe in a time-consuming, multistep procedure that is prone to alignment errors. In principle, such low-NA performance can also be achieved with BLPs if probe diameter is not a limitation, but much larger ball lens sizes are required to achieve comparable performance (see Section II). Based on
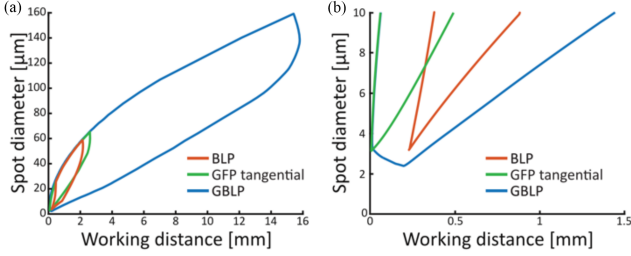
Fig. 3. Results revealing superior performance of the GBLP design. (a) Performance comparison of GBLP (bounded by blue curve) vs. BLP (red curve) and GFP (green curve) with improved working distance across the entire range of spots diameters. (b) Zoom of (a) over the high resolution range (SD $\leq$ 10 μm).
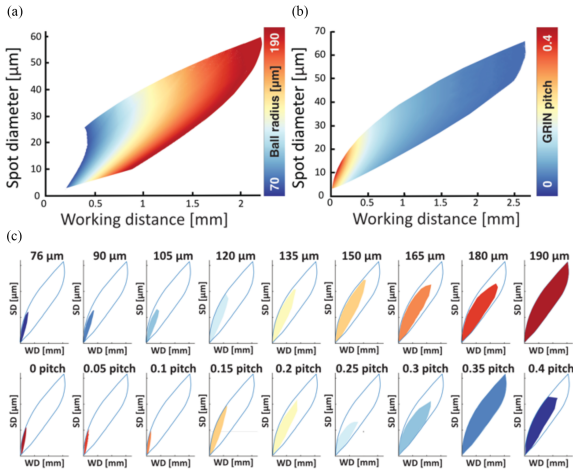

Fig. 4. Influence of the GRIN-fiber length and ball-lens size on the performance of the BLP (a), GFP (b), and GBLP (c). For GBLP, the impact of ball-lens size is presented in the top row of (c) using color fills to match the color scale in (a) and the impact of GRIN pitch is presented in the bottom row of (c) with color fills matching the color scale in (b). The solid blue curve in all plots of (c) corresponds to the full space of GBLP performance for reference (see Fig. 3(a)).

our simulations, WDs greater than 10 mm are available for spot diameters of $\geq$70 μm, which might be useful for applications such as imaging/ranging in the upper airway [24], [6] or in other large-diameter hollow organs.

In the intermediate and low-resolution ranges (spot diameters > 10 μm), we observe superior WD performance of the GBLP when compared to the GFP and BLP. As well, high-resolution probes (spot sizes of $\leq$ 10 μm shown in Fig. 3(b)) can be realized with equivalent or longer WD using the GBLP design. The gain in WD provided by the GBLP is discussed in detail the following sections.

1) Influence of Probe Components: To further support our analysis and conclusions, we studied the influence of each of the probe components on the imaging performance. For BLP and GFP, we focused on the impact of the ball-lens radius and GRIN-fiber pitch length, respectively. The scatterplot, after including the WD criterion, is color-coded according to the values of interest. It is clear from Fig. 4(a) that the BLP design reaches its optimal WD performance for a given spot size with the biggest ball lenses (simulated radius of 190 μm). Increasing

the GRIN pitch improves the resolution of the GFP (Fig. 4(b)) at the price of a significant reduction in the WD.

It is not possible to visualize in the same way the impact of the ball-lens radius and GRIN-fiber pitch on the GBLP performance. Therefore, we decided to show the available output beam parameters for selected values of ball-lens radius (Fig. 4(c) top row) and GRIN pitch (Fig. 4(c) bottom row) colored to match the color scales used for BLP and GFP in Fig. 4(a)–(b). To provide a reference, we plotted GBLP performance as a solid boundary shape (blue solid curve in Fig. 4(c)).

A GRIN pitch of 0.35, assuming all other dimensions of the probe can be varied, offers the full spectrum of GBLP realizations – from low-NA applications to high-resolution ones. On the other hand, the full range of GBLP realizations is available only for the largest ball lens simulated (190-μm radius). Interestingly, if high resolution is the primary requirement for probe performance, a wider range of GRIN pitches (0.15 to 0.4) and ball-lens sizes (>120 μm radius) can be used. This is further discussed in Section II.

2) Working Distance Gain: For a more comprehensive view of the superior performance of the GBPL, we performed a quantitative analysis of our simulated data. For each spot diameter, we calculated the working distance percentage gain versus BLP or GFP, defined respectively as:

$$WD\ GAIN_{BLP,GFP}\ (SD) = 100*$$
$$\times \frac{WD_{GBLP}\ (SD) - WD_{BLP,GFP}\ (SD)}{WD_{BLP,GFP}\ (SD)} \quad (2)$$

where $WD_{GBLP}(SD)$, $WD_{BLP}(SD)$, and $WD_{GFP}(SD)$ are maximum working distances extracted from boundary plots for given spot diameters for GBLP, BLP, and GFP, respectively. Calculations cover only the SD range provided by GFP (tangential plane) and BLP designs. The percentage gain of working distance when GBLP is compared with BLP monotonically increases from ~20% gain at smaller spot diameters to more than 200% gain for SD >35 μm (Fig. 5(a) – red curve). We note that the discontinuity in the shape of this curve is due to the limited range of ball lens radii included in the model (see Table I), however, this does not impact the overall trend.

A similar comparison of GBLP and GFP (tangential plane) reveals a 190% or higher gain for the whole range of spot diameters achievable for the GFP design (Fig. 5(a) – green curve). It must be noted that GBLP offers additional probe realizations with large spot diameters not available for GFP (>66 μm).

As the BLP offers improved performance compared with the GFP, especially for higher resolutions (smaller SD), and is less prone to astigmatism when a side-viewing design is used, we performed further comparison only between BLP and GBLP. From all the GBLP results, for a given value of SD, we extracted those specific configurations that offer better WD. In Fig. 5(b), we present the smallest ball-lens radius (blue curve) that provides longer WDs than the longest achieved using BLP for a given SD. In general, superior WD performance can be achieved with less than half the ball lens radius of the corresponding BLP (blue curve vs. black dotted curve in Fig. 5(b)). Even for the highest resolution range, the WD gain
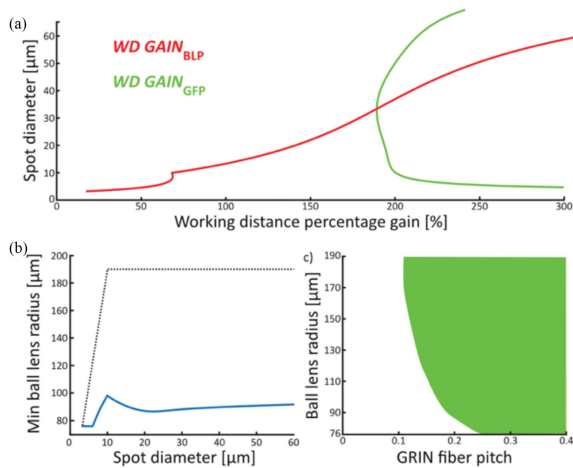
Fig. 5. Advantages of GBLP design in comparison with BLP and GFP. (a) The relationship between the gain in the working distance and spot diameter when GBLP is compared with BLP (red curve), or with GFP (green curve). (b) The smallest GBLP ball-lens radius that can be used to achieve a given spot size with superior WD performance when compared with BLP. The dotted curve indicates the corresponding ball-lens radius for maximum WD at a given SD for the BLP probe. (c) The range of GRIN pitch and ball-lens radius values for which WD performance of GLBP is superior (green fill).
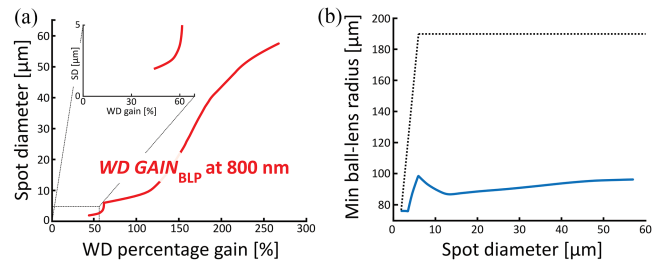

Fig. 6. Advantages of GBLP design in comparison with BLP for a simulated wavelength of 800 nm. (a) A gain in the working distance (GBLP vs. BLP) is observed for the whole range of spot diameters (inset – zoom on high resolution range). (b) Similarly, as for 1300 nm (Fig. 5(b)), GBLP allows designs with superior WD performance, but with a much smaller ball-lens radius. The dotted curve indicates the corresponding ball-lens radius for optimal WD at the given SD for the 800-nm BLP design.

is not the biggest advantage of the GBLP design; one can use much smaller sizes of the ball-lens element, which is the major size-limiting factor for both probe types: at 80-μm radius, the ball-lens diameter still exceeds that of typical uncoated single-mode fiber (125 μm). The only exception is for the smallest available SD (3.1 μm), where both probe designs reach the best WD for the same ball lens size (76 μm radius), but still with ~20% WD percentage gain of the GBLP design.

Additionally, we extracted the GRIN-fiber pitch and ball-lens radius values that correspond to the same or better WD performance of GBLPs compared to BLPs (Fig. 5(c)). As expected, for optimal working distance performance, one should avoid GRIN pitches <0.1. Essentially, future simulations and fabrication could be narrowed to GRIN pitch values >0.25. The sensitivity of GBLP designs to GRIN pitch variations is discussed in detail in Section IV C.

B. GBLP As a Design for Micro-Endomicroscopes

The development of imaging micro-endomicroscopes, defined as probes that are smaller than 0.5 mm in diameter and offer cellular level resolution (2 μm or better), is an emerging field that is expected to enable new biological measurements [11]. The design of such probes is made more challenging due to the physical constraints (set by the higher NA required) on the SD and WD for such small-diameter probes. The advantages of the GBLP highlighted here and applied to any imaging system with a central wavelength of around 800 nm could be a crucial step towards achieving cellular-resolution probes while maintaining a small probe size. In the 800-nm wavelength range, GBLP offers superior WD performance (Fig. 6(a)). For the most interesting high-resolution range of spot diameters smaller than 5 μm (Fig. 9(a) inset), the WD gain is greater than 45%. There is, moreover, the improvement that GBLP can provide for

micro-endomicroscope users in minimizing probe diameter. For our GBLP, we extracted the smallest possible ball-lens radius that offers the same or better WD performance for a given SD when compared with BLP (Fig. 6(b)). Results indicate that a GBLP with much smaller ball-lens radius (half of the BLP radius for most of the SD range) can be used to achieve the same or better SD and WD performance when compared with BLP, making our hybrid probe design an interesting solution for future micro-endomicroscopes. Again, as for 1300-nm designs, there is a ball-lens size advantage except for the highest resolution (1.5 μm). We clearly see the potential of GBLP micro-endomicroscopes for high-resolution OCT imaging, however, other imaging techniques such as fluorescence imaging and Raman spectroscopic imaging would benefit from similarly designed micro-endomicroscopes due to the small probe sizes that can be achieved.

Comparison of the best resolution, extracted from simulation results, suggests only a slight advantage of GBLP when compared with BLP when working in air (1.4 μm for GBLP versus 1.5 μm for BLP). Interestingly, a similar analysis of probes working in a water environment (results not shown), reveals a much greater advantage of the GBLP design (best resolution of 2.1 μm for GBLP compared with 14.3 μm for BLP). The impact of the surrounding medium is discussed further in Section IV.B.

IV. DISCUSSION

A. GRIN Fiber Parameters

Various GRIN fibers can be used to fabricate GBLPs and GFPs. For GFPs, there is a clear advantage to using larger core GRIN fiber (Fig. 7(a)). If smaller core GRIN fiber is used, we observe a significant drop in WD performance (light green fill vs. region within solid green curve in Fig. 7(a)). This advantage fades away for GBLP, where smaller core GRIN GBLPs perform worse only for very low-NA realizations (light blue fill vs. solid blue curve in Fig. 7(b)). We note that small-core GRIN fibers are more readily available, and the only GRIN fiber with a near-perfect parabolic refractive-index profile we are aware of has a small 62.5-μm core diameter.

Another aspect that might impact the accuracy of the ABCD simulations is the aperture diffraction effect, which cannot be

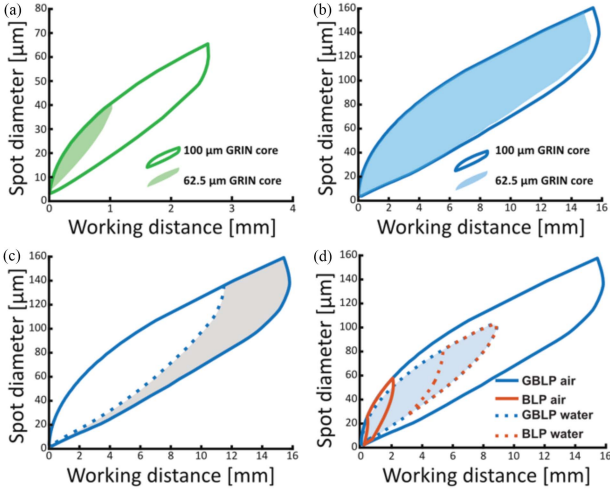Fig. 7. Impact of GRIN-fiber core diameters and surrounding medium on probe performance. (a) GFP tangential plane performance for 100-μm GRIN core (region bounded by light green fill) and 62.5-μm GRIN core (solid green curve). (b) GBLP performance for 100-μm GRIN core (light blue fill) and 62.5-μm GRIN core (solid blue curve). (c) The range of GBLP designs that may be impacted by the aperture diffraction effect (shaded gray). (d) Impact of surrounding medium refractive index on the performance of the BLP and GBLP. Solid curves: blue for GBLP and red for BLP working in the air. Dotted curves: Performance of the probe working in a medium of higher refractive index ($n = 1.32$ for water [26]). For clarity, GBLP solutions for higher refractive index are also marked with a light blue fill.

neglected when the beam diameter at the entrance of the GRIN fiber section approaches the size of the entrance aperture of the GRIN fiber (the core diameter). When the beam waist ω_0 approaches the GRIN-fiber core diameter (more precisely, when $\omega_0/R_{\text{GRIN CORE}} > 0.64$), the accuracy of the ABCD matrix method decreases [23]. Results that are potentially affected by the aperture effect are colored gray in Fig. 7(c). Again, this effect mainly impacts lower NA probe realizations. We believe those performance regions are still potentially available but require validation using more sophisticated modeling methods (e.g., BPM) [23], [25] to support the ABCD matrix method to explore the expected properties of the output beam more accurately.

B. Surrounding Medium

One factor to be considered when selecting the optimal probe design is the impact of the surrounding medium on the probe performance. For example, if a fiber probe is inserted directly into tissue, the focusing power of a refractive surface such as a ball lens is dramatically reduced. For BLPs, the range of achievable performance is greatly reduced, and high-resolution imaging is much more difficult to achieve. Conversely, the performance of GFPs is improved; while the minimum achievable SD is larger than in air (similarly as for 800 nm probes - see Section III.B.), the difference in beam size between the tangential and sagittal planes is reduced. At 1300 nm, the smallest achievable spot size for the BLP is 2.5 μm in air and 26.5 μm in water, whereas, for the GBPL, it is 2.4 μm in air and 3.5 μm in water. The added segment of GRIN fiber in the GBLP design mitigates the loss of focusing power from the ball lens when immersed in a medium with a higher refractive index (Fig. 7(d)).
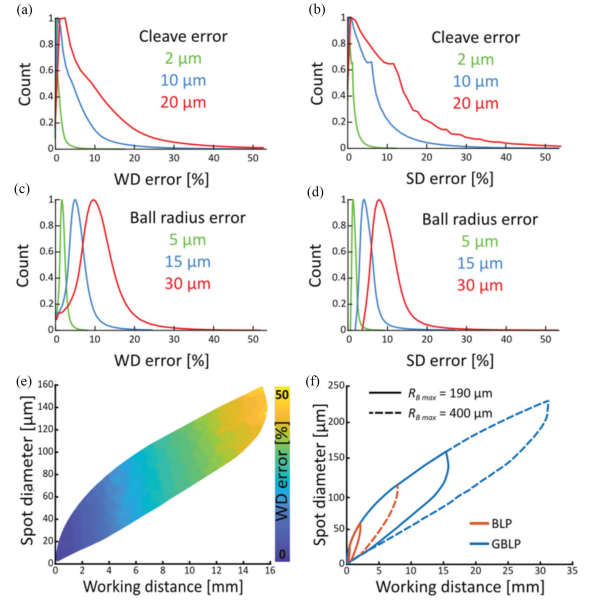

Fig. 8. GBLP performance error due to inaccuracy in fabrication. Histogram distribution fits (MATLAB, nonparametric kernel-smoothing distribution) corresponding to the impact of GRIN cleaving accuracy on WD (a) and SD (b) errors, and the impact of ball-lens radius fabrication accuracy on WD (c) and SD (d) errors. In (e), a plot of WD error as a function of SD and WD is shown. For (a) and (b), colors indicate GRIN fiber cleave error of 2 μm (green), 10 μm (blue), and 20 μm (red). For (c) and (d), colors indicate ball-lens fabrication error (radius) of 5 μm (green), 15 μm (blue) and 30 μm (red). In (f) we compare BLP (red) and GBLP (blue) performance for maximum ball-lens sizes simulated of $R_{B\ max} = 190$ μm (solid) and $R_{B\ max} = 400$ μm (dotted).

C. Fabrication Accuracy

Our experience in probe fabrication suggests that tolerances of ~10 μm for GRIN-fiber length and ~15 μm for ball-lens radius are readily achievable. Such precision in cleaving the fiber to a specific length can be further improved at the cost of fabrication time. One way to achieve this is to pre-cleave the fiber section to a length longer than required and slowly reduce the length using a polishing process.

Using ABCD simulation data, we estimated the influence of the fabrication accuracy (GRIN-fiber length and ball-lens radius) on GBLP probe performance (both SD and WD). Inaccuracy in GRIN-fiber length cleaving of 10 μm (either shorter or longer) translates to SD and WD error of less than 30% (Fig. 8(a) and (b) – blue histogram fit). The deviation in ball-lens radius of 15 μm (either smaller or larger) will lead to WD errors of less than 20% and SD errors less then 15% (Fig. 8(c) and (d) – blue histogram fit). For reference, we added the SD and WD errors assuming improved fabrication accuracy (2 μm for GRIN length and 5 μm for ball-lens radius – green histogram fits on Fig. 8(a)–(d), as well as less accurate fabrication (20 μm for GRIN length and 30 μm for ball-lens radius – red histogram fits on Fig. 8(a)-(d).

Overall, our analysis of the fabrication accuracy-based performance error reveals that the largest errors are present for low-NA probe realizations (as shown in Fig. 8(e)).

As emphasized previously, in this work, we focus on small footprint probes. We have experience in the accurate and repeatable fabrication of ball lenses with a radius up to $R_{B\ max}$

$= 190$ μm. One can make efforts to fabricate ball lenses with a greater radius trading off the size accuracy and repeatability. BLP, when simulated for $R_{B\ max} = 400$ μm, offers also low-NA solutions suitable for large hollow organ measurements (Fig. 8(f) red dotted shape). Regardless of the maximum ball-lens size used in simulations, we observe improved WD performance of GBLP when compared with BLP (Fig. 8(f) blue dotted shape). Additionally, the same spot sizes can be achieved with 2-3 times smaller ball-lens diameters using a GBLP design.

It is a challenge to fabricate a perfectly spherical ball lens. Especially for the largest ball radii, asymmetries in probe dimensions are readily observed. We tested the idea of rotating the probe during ball lens fabrication and found it effective in providing the most symmetric ball lenses. Alternatively, sometimes asymmetry in ball lens shape is desired. For instance, to reduce the influence of the catheter tubing on astigmatism, an ellipsoidal ball lens can be created by positioning the fusion splicer vertically during the fabrication process [27].

When fabricating a GBLP, the cleaved GRIN length is the most sensitive parameter, and 10-20 μm variations can make a big difference in the resulting spot size/WD. However, any error in GRIN length can be compensated during ball lens fabrication. As already mentioned, if the GRIN section is too long, it can be polished to the proper length; on the other hand, if the GRIN length is too short, then the diameter of the ball lens can be adjusted (reduced) to still achieve the desired spot size at an only minimally altered WD. This is an advantage of a probe with two focusing elements – the second element can be adjusted to compensate for any error in the first element.

D. GBLP Vs Other Fiber Probes

In previous sections, we presented the superior performance of GBLP when compared with BLP and GFP designs. As mentioned, GFPs, if not used with index matching media, suffer from significant astigmatism. In a recent paper, the authors reported GFP designs with various spot sizes [27]. For spot diameters of 20.2 μm, 35.1 μm and 59.4 μm, working distances of 1.6 mm, 2.9 mm and 4.2 mm, respectively, were presented. In comparison, for the same spot diameters, our GBLP design offers WDs of >3 mm, >5mm and >8 mm, respectively. If an all-fiber configuration and small footprint are not required, one may consider GRIN lens-based probes. Numerically simulated single or dual GRIN probes working at a 30-μm spot diameter can provide $\sim$3.2-times better working distance performance than GBLP designs at the expense of 2.6 times larger probe diameter and far more difficult fabrication [22]. Interestingly, some researchers have suggested that C-lenses (cylindrical, single-refractive index, refractive lenses) might be a better choice than GRIN lenses for long-WD imaging probes [28].

BLPs are closer in performance to GBLPs and do not suffer from astigmatism when used for side viewing. In one interesting work, as described above, ball lenses were fabricated to be ellipsoidal to counterbalance the astigmatism caused by the catheter tubing [29]. We estimate the WD of the presented probes to be $\sim$1.65 mm; for GBLPs producing the same spot diameter (28.5 μm), the WD is greater than 4 mm. The advantage of GBLPs

at the highest resolutions, however, is not as significant as for other resolution ranges. In two papers from the X. Li group, two high-resolution BLPs were experimentally presented: 6.2 μm spot size with 545 μm working distance and 5.7 μm with $\sim$600 μm working distance [17], [30]. A GBLP with the same spot size, 6.2 μm, offers close to 800-μm working distance and, at 5.7 μm spot size, a WD >750 μm. Another monolithic BLP probe with a thin gold layer was presented for common path interferometry [31]. For a spot diameter of 42.5 μm, a WD of 3 mm was measured; whereas, a GBLP with the same spot size provides >6 mm WD. An anastigmatic ultrathin BLP encapsulated inside a 26-gauge hypodermic needle with $\sim$19-μm spot size was fabricated for a swept-source OCT system [32]. The working distance was experimentally measured to be 0.62 mm; much smaller than the 2.9-mm WD for a GBLP at the same spot size.

Considering non-standard fiber imaging probes, a particular group of designs with multiple GRIN fiber sections and various phase masks has attracted the interest of researchers seeking to achieve an extended depth of focus. Since the beam is no longer Gaussian in such cases, it is difficult to compare directly with a GBLP design. For instance, Liu and colleagues [21] reported a probe with measured 4.4-μm spot diameter, twofold focus extension and 1.7 times gain in working distance compared with a GFP with the same spot size. From our simulations, we estimate that for a GBLP with the same spot diameter of 4.4 μm, a WD gain of 4 is expected when compared to a GFP. In earlier work by Lorenser et al., a probe with 6.5 μm spot diameter, depth of focus (DOF) gain of $\sim$2 and WD of $\sim$500 μm was presented [20]. A GBLP at this lateral resolution offers no DOF gain, but better working distance of $\sim$850 μm. One should keep in mind that focus extension comes with an SNR penalty and reduced contrast when compared with Gaussian beam probes [33], [34]. Another way to extend the focus is by inserting a GRIN fiber between a single-mode fiber and an axicon fabricated on the tip of no-core fiber [35]. DOF gain of 5.2 was reported for a 2-μm spot diameter, however, the working distance starts essentially just after the axicon tip.

Fascinating approaches for fabrication of fiber probes of the future include the use of freeform optics and metamaterials. In both cases, the final surface of the probe can be designed to remove astigmatism introduced by the probe's encapsulating tubing. Using an optical 3D microprinting method, an aberration-corrected miniature probe was fabricated with a spot size of 12.4 μm and working distance of $\sim$ 740 μm (from the freeform optic surface). A GBLP would provide $\sim$1.8 mm working distance at the same spot size, however, without compensating for the astigmatism caused by the tubing. Even more impressive, from the perspective of imaging resolution, is the metalens-based probe presented for nearly diffraction-limited imaging of lung samples. The metalens, fabricated at the last probe interface, modifies the phase of the incident beam to enable imaging with 6.4 μm lateral resolution and WD of 0.5 mm [36]. In comparison, a GBLP with the same resolution provides a WD of 0.87 mm.

Finally, as already mentioned, the GBLP design presented in this work has been already experimentally validated in the low-NA regime [19]. The authors presented their hybrid probe with diameter greater than 0.5 mm and WD of >14 mm. The

GBLP shares the same multiple element design as demonstrated in the low-NA regime, but in the work presented here we have shown that the combined GRIN-ball lens design offers much more.

V. CONCLUSION

In summary, we have presented the superior performance of the double-refractive-element GRIN-fiber-and-ball-lens probe design over a wide range of system performance parameters, when compared to classical GRIN-fiber probes and ball-lens probes. For intuitive visualization of the probe design performance, we introduced a novel means of comprehensively presenting the simulation results, especially suitable when more than two simulation variables are used.

GBLP offers access to long-working-distance low-NA applications with smaller probe size and simplified fabrication. Moreover, a gain in WD performance is apparent for a whole range of NAs, including high-NA designs. The superior WD performance of the GBLP design is especially promising for applications of side-viewing probes encased in a catheter or needle.

Our analysis of the impact of GRIN-fiber length and ball-lens size leads to some interesting conclusions: the GRIN pitch can be kept within the range 0.25-0.4 whilst maintaining optimal GBLP performance (Fig. 5(c)); even when the WD gain is not as prominent for high-NA GBLPs, we demonstrated that designs with half the ball-lens radius could achieve the same or better WD performance.

We presented error estimation in the designed working distances caused by fabrication inaccuracies, finding that the most significant errors are present for low-NA probe solutions.

We confirmed by simulation at a wavelength of 800 nm that the GBLP offers superior WD performance at half the ball lens radius (as for 1300 nm). Moreover, the GBLP provides in this wavelength range a higher maximum resolution when compared to the BLP and the maximum resolution is better preserved when the probe is used in media with a higher refractive index.

Overall, we demonstrated the potential of GBLP designs for extended working distance applications, especially important for side-viewing probes, with a highly reduced impact of medium refractive index and a much smaller footprint compared with BLP or GFP designs. These advantages make the GBLP a tool well worth implementing for a suite of new biological measurements using micro-endomicroscopes.

REFERENCES

[1] U. Utzinger and R. R. Richards-Kortum, "Fiber optic probes for biomedical optical spectroscopy," *J. Biomed. Opt.*, vol. 8, no. 1, pp. 121–147, 2003, doi: 10.1117/1.1528207.

[2] I. Latka, S. Dochow, C. Krafft, B. Dietzek, and J. Popp, "Fiber optic probes for linear and nonlinear Raman applications – current trends and future development," *Laser Photon. Rev.*, vol. 7, no. 5, pp. 698–731, Sep. 2013, doi: 10.1002/LPOR.201200049.

[3] D. Lorenser, R. A. McLaughlin, and D. D. Sampson, "Optical coherence tomography in a needle format," in *Optical Coherence Tomography: Technology and Applications*, 2nd ed., W. Drexler and J. G. Fujimoto, Eds. Cham, Switzerland: Springer, 2015, pp. 2413–2472. doi: 10.1007/978-3-319-06419-2_83.

[4] H. H. Joo, M. J. Cobb, M. B. Kimmey, and X. Li, "Optical coherence tomography imaging of the pancreas: A needle-based approach," *Clin. Gastroenterol. Hepatol.*, vol. 3, no. 7, pp. S49–S52, Jul. 2005, doi: 10.1016/S1542-3565(05)00259-4.

[5] B. F. Kennedy, D. D. Sampson, K. M. Kennedy, and R. A. McLaughlin, "Needle optical coherence elastography for tissue boundary detection," *Opt. Lett.*, vol. 37, no. 12, pp. 2310–2312, Jun. 2012, doi: 10.1364/OL.37.002310.

[6] J. J. Armstrong, M. S. Leigh, D. D. Sampson, J. H. Walsh, D. R. Hillman, and P. R. Eastwood, "Quantitative upper airway imaging with anatomic optical coherence tomography," *Amer. J. Respir. Crit. Care Med.*, vol. 173, no. 2, pp. 226–233, Dec. 2006, doi: 10.1164/RCCM.200507-1148OC.

[7] E. Breatnach, G. C. Abbott, and R. G. Fraser, "Dimensions of the normal human trachea," *Amer. J. Roentgenol.*, vol. 142, no. 5, pp. 903–906, 1984, doi: 10.2214/AJR.142.5.903.

[8] J. P. Williamson et al., "Measuring airway dimensions during bronchoscopy using anatomical optical coherence tomography," *Eur. Respir. J.*, vol. 35, no. 1, pp. 34–41, Jan. 2010, doi: 10.1183/09031936.00041809.

[9] B. E. Bouma, K. Otsuka, M. Villiger, and W.-Y. Oh, "Intravascular optical coherence tomography," *Biomed. Opt. Exp.*, vol. 8, no. 5, pp. 2660–2686, May 2017, doi: 10.1364/BOE.8.002660.

[10] M. J. Gora et al., "Tethered capsule endomicroscopy enables less-invasive imaging of gastrointestinal tract microstructure," *Nature Med.*, vol. 19, no. 2, Feb. 2013, Art. no. 238, doi: 10.1038/NM.3052.

[11] G. R. Untracht, K. Karnowski, and D. D. Sampson, "Imaging the small with the small: Prospects for photonics in micro-endomicroscopy for minimally invasive cellular-resolution bioimaging," *APL Photon.*, vol. 6, no. 6, Jun. 2021, Art. no. 060901, doi: 10.1063/5.0052258.

[12] A. C. Loy et al., "Anatomic optical coherence tomography of upper airways," in *Optical Coherence Tomography Technology and Applications*, W. Drexler and J. G. Fujimoto, Eds. New York City, NY, USA: Springer, 2015, pp. 2245–2262. doi: 10.1007/978-3-319-06419-2_77.

[13] S. Ohayon et al., "Minimally invasive multimode optical fiber microendoscope for deep brain fluorescence imaging," *Biomed. Opt. Exp.*, vol. 9, no. 4, pp. 1492–1509, Apr. 2018, doi: 10.1364/BOE.9.001492.

[14] C. Wang, F. Zhang, S. B. Bi, X. Q. Xia, and T. T. Xu, "Fabrication method of ultra-small gradient-index fiber probe," *Adv. Manuf.*, vol. 2, no. 4, pp. 327–332, Oct. 2014, doi: 10.1007/s40436-014-0089-7.

[15] K. Singh, D. Yamada, and G. Tearney, "Astigmatism corrected common path probe for optical coherence tomography," *Lasers Surg. Med.*, vol. 49, no. 3, pp. 312–318, Mar. 2017, doi: 10.1002/LSM.22554.

[16] H. S. Cho et al., "High frame-rate intravascular optical frequency-domain imaging in vivo," *Biomed. Opt. Exp.*, vol. 5, no. 1, 2014, Art. no. 223, doi: 10.1364/BOE.5.000223.

[17] W. Yuan, R. Brown, W. Mitzner, L. Yarmus, and X. Li, "Super-achromatic monolithic microprobe for ultrahigh-resolution endoscopic optical coherence tomography at 800 nm," *Nature Commun.*, vol. 8, no. 1, pp. 1–9, Nov. 2017, doi: 10.1038/s41467-017-01494-4.

[18] Y. Zhang and H. Gross, "Systematic design of microscope objectives. Part II: Lens modules and design principles," *Adv. Opt. Technol.*, vol. 8, no. 5, pp. 349–384, Oct. 2019, doi: 10.1515/aot-2019-0013.

[19] S. Balakrishnan and A. L. Oldenburg, "All-fiber probes for endoscopic optical coherence tomography of the large airways," *Appl. Opt.*, vol. 60, no. 22, Aug. 2021, Art. no. 6385, doi: 10.1364/ao.431010.

[20] D. Lorenser, X. Yang, and D. D. Sampson, "Ultrathin fiber probes with extended depth of focus for optical coherence tomography," *Opt. Lett.*, vol. 37, no. 10, pp. 1616–1618, May 2012, doi: 10.1364/OL.37.001616.

[21] J. Meng, J. Qiu, T. Han, Z. Ding, and Z. Liu, "Uniform focusing with an extended depth range and increased working distance for optical coherence tomography by an ultrathin monolith fiber probe," *Opt. Lett.*, vol. 45, no. 4, pp. 976–979, Feb. 2020, doi: 10.1364/OL.383428.

[22] W. Jung, W. Benalcazar, A. Ahmad, U. Sharma, H. Tu, and S. A. Boppart, "Numerical analysis of gradient index lens-based optical coherence tomography imaging probes," *J. Biomed. Opt.*, vol. 15, no. 6, 2010, Art. no. 066027, doi: 10.1117/1.3523374.

[23] D. Lorenser, X. Yang, and D. D. Sampson, "Accurate modeling and design of graded-index fiber probes for optical coherence tomography using the beam propagation method," *IEEE Photon. J.*, vol. 5, no. 2, Apr. 2013, Art. no. 3900015, doi: 10.1109/JPHOT.2013.2250939.

[24] J. J. Armstrong et al., "In vivo size and shape measurement of the human upper airway using endoscopic long-range optical coherence tomography," *Opt. Exp.*, vol. 11, no. 15, pp. 1817–1826, Jul. 2003, doi: 10.1364/OE.11.001817.

[25] J. Meng, J. Qiu, T. Han, Z. Ding, and Z. Liu, "Fast simulation and design of the fiber probe with a fiber-based pupil filter for optical coherence tomography using the eigenmode expansion approach," *Opt. Exp.*, vol. 29, no. 2, pp. 2172–2183, Jan. 2021, doi: 10.1364/OE.416279.

[26] H. Giessen, M. Vieweg, S. Kedenburg, and T. Gissibl, "Linear refractive index and absorption measurements of nonlinear optical liquids in the visible and near-infrared spectral region," *Opt. Mater. Exp.*, vol. 2, no. 11, pp. 1588–1611, Nov. 2012, doi: 10.1364/OME.2.001588.

[27] D.-S. Kim and S. Moon, "Optimized working distance of a micro-optic OCT imaging probe," *Curr. Opt. Photon.*, vol. 4, no. 4, pp. 330–335, Aug. 2020, doi: 10.1364/COPP.4.000330.

[28] Y. Fan, S. Luo, and H. Kang, "A comparison of the long working distance of the GRIN Lens- and C-Lens-based OCT probe," *IEEE Access*, vol. 7, pp. 93212–93218, 2019, doi: 10.1109/ACCESS.2019.2927501.

[29] H. S. Cho et al., "High frame-rate intravascular optical frequency-domain imaging in vivo," *Biomed. Opt. Exp.*, vol. 5, no. 1, pp. 223–232, Jan. 2014, doi: 10.1364/BOE.5.000223.

[30] W. Yuan et al., "Theranostic OCT microneedle for fast ultrahigh-resolution deep-brain imaging and efficient laser ablation in vivo," *Sci. Adv.*, vol. 6, no. 15, 2020, Art. no. eaaz9664, doi: 10.1126/SCIADV.AAZ9664/SUPPL_FILE/AAZ9664_SM.PDF.

[31] K. Blessing, S. Sharma, A. Gumann, and K. Singh, "Low cost scalable monolithic common path probe design for the application in endoscopic optical coherence tomography," *Eng. Res. Exp.*, vol. 1, no. 2, Oct. 2019, Art. no. 025008, doi: 10.1088/2631-8695/AB4783.

[32] T. Wu et al., "Ultrathin lensed fiber based anastigmatic needle probe for endoscopic swept source optical coherence tomography," *Opt. Lasers Eng.*, vol. 154, Jul. 2022, Art. no. 107043, doi: 10.1016/J.OPTLASENG.2022.107043.

[33] A. Curatolo et al., "Quantifying the influence of Bessel beams on image quality in optical coherence tomography," *Sci. Rep.*, vol. 6, no. 1, pp. 1–12, Mar. 2016, doi: 10.1038/srep23483.

[34] D. Lorenser, C. C. Singe, A. Curatolo, and D. D. Sampson, "Energy-efficient low-Fresnel-number Bessel beams and their application in optical coherence tomography," *Opt. Lett.*, vol. 39, no. 3, 2014, Art. no. 548, doi: 10.1364/OL.39.000548.

[35] B.-O. Guan, G. Wang, J. Ma, L. Cheng, and W. Wang, "Miniature all-fiber axicon probe with extended Bessel focus for optical coherence tomography," *Opt. Exp.*, vol. 27, no. 2, pp. 358–366, Jan. 2019, doi: 10.1364/OE.27.000358.

[36] H. Pahlevaninezhad et al., "Nano-optic endoscope for high-resolution optical coherence tomography in vivo," *Nature Photon.* vol. 12, no. 9, pp. 540–547, Jul. 2018, doi: 10.1038/s41566-018-0224-2.